Journal of Computational Physics **181,** 155–185 (2002)
doi:10.1006/jcph.2002.7117

On the Use of Higher-Order Finite-Difference Schemes on Curvilinear and Deforming Meshes

Miguel R.Visbal and Datta V. Gaitonde

Computational Sciences Branch, Aeronautical Sciences Division, Air Force Research Laboratory, Wright-Patterson AFB, Ohio 45433
E-mail: visbal@vaa.wpafb.af.mil

Received April 4, 2001; revised May 23, 2002

This study enables the use of very high-order finite-difference schemes for the solution of conservation laws on stretched, curvilinear, and deforming meshes. To illustrate these procedures, we focus on up to 6th-order Pade-type spatial discretizations coupled with up to 10th-order low-pass filters. These are combined with explicit and implicit time integration methods to examine wave propagation and wall-bounded flows described by the Navier–Stokes equations. It is shown that without the incorporation of the filter, application of the high-order compact scheme to nonsmooth meshes results in spurious oscillations which inhibit their applicability. Inclusion of the discriminating low-pass high-order filter restores the advantages of high-order approach even in the presence of large grid discontinuities. When three-dimensional curvilinear meshes are employed, the use of standard metric evaluation procedures significantly degrades accuracy since freestream preservation is violated. To overcome this problem, a simple technique is adopted which ensures metric cancellation and thus ensures freestream preservation even on highly distorted curvilinear meshes. For dynamically deforming grids, an effective numerical treatment is described to evaluate expressions containing the time-varying transformation metrics. With these techniques, metric cancellation is guaranteed regardless of the manner in which grid speeds are defined. The efficacy of the new procedures is demonstrated by solving several model problems as well as by application to flow past a rapidly pitching airfoil and past a flexible panel.

Key Words: high-order methods; compact differences; curvilinear coordinates.

1. INTRODUCTION

Despite significant progress in computational sciences, challenges persist in the accurate numerical simulation of a broad spectrum of dynamic, multiphysics phenomena. These challenging areas include the direct-numerical and large-eddy simulation of turbulence, aeroacoustics, fluid/structure interactions, and electromagnetics. One approach to reducing

0021-9991/02 $35.00

the severe computational requirements of standard low-order simulations is to employ higher-order formulations [1–3].

In the hierarchy of high-order methods, compact schemes represent an attractive choice for reducing dispersion and anisotropy errors. This is primarily due to their spectral-like resolution [2]. An additional advantage accrues from their ease of extension to multiple disciplines. In the context of fluid dynamics, these schemes have typically been used to examine flow fields on simple domains, which can be discretized by static Cartesian meshes (e.g., Refs. [2–4]). Calculations on practical geometries, however, usually require curvilinear and, in some cases, time-varying meshes of limited smoothness. In these cases, the advantage of high-order compact schemes remains to be characterized. It is clear that careful analysis of these issues is essential prior to the routine application of compact schemes to practical simulations. We focus therefore on the following aspects:

- Impact of mesh quality: Body-fitted grids for complex configurations contain non-smooth features such as slope discontinuities, skewness, and stretching. The impact of these factors on scheme performance can be significant. It has been shown that the standard explicit second-order scheme incurs large error at locations where the mesh spacing changes suddenly [5]. Consequently, it is natural to inquire whether the spatially implicit character of compact-difference formulas accentuates this effect to the point that advantages over cheaper lower-order schemes is lost. The question is addressed by considering meshes with sudden discontinuities in spacing and rapid sustained metric variation. In these cases, we demonstrate the crucial role played by the filtering technique, previously described in Refs. [2, 6, 7], in enforcing stability while retaining the absolute accuracy advantages over lower-order methods.
- Freestream preservation: Finite-difference procedures for solving the governing equations in strong conservation form require special treatment to preserve the freestream in 3-D curvilinear meshes. For lower-order schemes, this aspect has been investigated extensively in Refs. [8]–[10] while for higher-order schemes in two-dimensional situations, the issue has been examined in Ref. [6]. It is demonstrated later that in contrast to 2-D situations, straightforward methods of computing higher-order metrics in 3-D can cause unacceptably large errors even on relatively benign but curvilinear meshes. To alleviate this difficulty, this work adopts and validates metric evaluation techniques to guarantee freestream preservation with higher-order algorithms.
- Application to moving and deforming meshes: Another area where high-order compact solvers have not been employed or systematically evaluated is in the context of simulations requiring dynamic (or moving) meshes. In this case also, the requirement that the geometric conservation law be satisfied mandates the use of carefully designed metric evaluation techniques. A simple yet powerful procedure is developed for both spatial and time metric terms to ensure that the higher-order approach retains its advantages over lower-order schemes.

Details of the governing equations are given in Section 2. The numerical procedure comprises two main components: the spatial discretization and the higher-order low-pass filter. Both are described together with the explicit and implicit time-integration methods in Section 3. The impact of mesh quality on the performance of higher-order discretizations is examined in Section 4.1. The techniques required to ensure freestream preservation in static three-dimensional curvilinear meshes are developed and demonstrated in Section 4.2. The treatment of moving mesh metric evaluation and enforcement of geometric conservation law are presented in Section 4.3. Finally, two applications are presented, the first addressing dynamic stall over a pitching airfoil (Section 4.4) and the second simulating fluttering of a flexible panel (Section 4.5).

2. GOVERNING EQUATIONS

In order to develop a procedure suitable for nonlinear fluid dynamic, aeroacoustic, and aeroelastic applications over complex configurations, the full Navier–Stokes equations are selected and are cast in strong conservative form after introducing a general time-dependent curvilinear coordinate transformation $(x, y, z, t) \rightarrow (\xi, \eta, \zeta, \tau)$ [8, 11, 12]. In vector notation, and in terms of nondimensional variables, these equations are

$$\frac{\partial}{\partial \tau}\left(\frac{\vec{U}}{J}\right) + \frac{\partial \hat{F}}{\partial \xi} + \frac{\partial \hat{G}}{\partial \eta} + \frac{\partial \hat{H}}{\partial \zeta} = \frac{1}{Re}\left[\frac{\partial \hat{F}_v}{\partial \xi} + \frac{\partial \hat{G}_v}{\partial \eta} + \frac{\partial \hat{H}_v}{\partial \zeta}\right]. \tag{1}$$

Here $\vec{U} = \{\rho, \rho u, \rho v, \rho w, \rho E\}$ denotes the solution vector and $J = \partial(\xi, \eta, \zeta, \tau)/\partial(x, y, z, t)$ is the transformation Jacobian. The inviscid fluxes $\hat{F}$, $\hat{G}$ and $\hat{H}$ are

$$\hat{F} = \begin{bmatrix} \rho\hat{U} \\ \rho u\hat{U} + \hat{\xi}_x p \\ \rho v\hat{U} + \hat{\xi}_y p \\ \rho w\hat{U} + \hat{\xi}_z p \\ (\rho E + p)\hat{U} - \hat{\xi}_t p \end{bmatrix} \tag{2}$$

$$\hat{G} = \begin{bmatrix} \rho\hat{V} \\ \rho u\hat{V} + \hat{\eta}_x p \\ \rho v\hat{V} + \hat{\eta}_y p \\ \rho w\hat{V} + \hat{\eta}_z p \\ (\rho E + p)\hat{V} - \hat{\eta}_t p \end{bmatrix} \tag{3}$$

$$\hat{H} = \begin{bmatrix} \rho\hat{W} \\ \rho u\hat{W} + \hat{\zeta}_x p \\ \rho v\hat{W} + \hat{\zeta}_y p \\ \rho w\hat{W} + \hat{\zeta}_z p \\ (\rho E + p)\hat{W} - \hat{\zeta}_t p \end{bmatrix}, \tag{4}$$

where

$$\hat{U} = \hat{\xi}_t + \hat{\xi}_x u + \hat{\xi}_y v + \hat{\xi}_z w \tag{5}$$

$$\hat{V} = \hat{\eta}_t + \hat{\eta}_x u + \hat{\eta}_y v + \hat{\eta}_z w \tag{6}$$

$$\hat{W} = \hat{\zeta}_t + \hat{\zeta}_x u + \hat{\zeta}_y v + \hat{\zeta}_z w \tag{7}$$

$$E = \frac{T}{(\gamma - 1)M_\infty^2} + \frac{1}{2}(u^2 + v^2 + w^2). \tag{8}$$

Here, $\hat{\xi}_x = J^{-1}\partial\xi/\partial x$ with similar definitions for the other metric quantities. The viscous fluxes, $\hat{F}_v$, $\hat{G}_v$, and $\hat{H}_v$ (which do not involve the time metrics) can be found, for instance, in Ref. [13]. In the expressions above, u, v, w are the Cartesian velocity components, ρ the density, p the pressure, and T the temperature. The perfect gas relationship $p = \rho T/\gamma M_\infty^2$ is also assumed. All flow variables have been normalized by their respective freestream values except for pressure, which has been nondimensionalized by $\rho_\infty u_\infty^2$.

In deriving the strong-conservation form of the flow equations, the following metric identities have been implicitly invoked,

$$I_1 = (\hat{\xi}_x)_\xi + (\hat{\eta}_x)_\eta + (\hat{\zeta}_x)_\zeta = 0 \tag{9}$$

$$I_2 = (\hat{\xi}_y)_\xi + (\hat{\eta}_y)_\eta + (\hat{\zeta}_y)_\zeta = 0 \tag{10}$$

$$I_3 = (\hat{\xi}_z)_\xi + (\hat{\eta}_z)_\eta + (\hat{\zeta}_z)_\zeta = 0 \tag{11}$$

$$I_4 = (1/J)_\tau + (\hat{\xi}_t)_\xi + (\hat{\eta}_t)_\eta + (\hat{\zeta}_t)_\zeta = 0, \tag{12}$$

where again, subscripts denote partial derivatives. The first three identities constitute a differential statement of surface conservation for a closed cell. The last metric identity (I_4) expresses volume conservation and is referred to in the literature as the geometric conservation law (GCL) [10]. In a finite-difference discretization, these identities must be satisfied numerically in order to ensure freestream preservation. For time-invariant coordinate transformations (i.e., nonmoving meshes), only the first three identities are applicable.

3. NUMERICAL METHOD

3.1. Spatial Discretization

A finite-difference approach is employed to discretize the above equations. This choice is motivated by the relative ease of formal extension to higher-order accuracy. For any scalar pointwise discrete quantity, ϕ, such as a metric, flux component or flow variable, the spatial derivative ϕ' is obtained in the transformed plane by solving the tridiagonal system

$$\alpha\phi'_{i-1} + \phi'_i + \alpha\phi'_{i+1} = b\frac{\phi_{i+2} - \phi_{i-2}}{4\Delta\xi} + a\frac{\phi_{i+1} - \phi_{i-1}}{2\Delta\xi}, \tag{13}$$

where α, a, and b determine the spatial properties of the algorithm. The formula encompasses a family of schemes ranging in accuracy from the standard three-point, second-order explicit method (*E2*) to the compact five-point, sixth-order algorithm (*C6*) [2]. The coefficients for the schemes considered are presented in Table I. A discussion of the

TABLE I
Schemes with Five-Point Stencil (Eq. (13))

Scheme	α	a	b	OA
E2	0	1	0	2
E4	0	$\frac{4}{3}$	$\frac{-1}{3}$	4
C4	$\frac{1}{4}$	$\frac{3}{2}$	0	4
C6	$\frac{1}{3}$	$\frac{14}{9}$	$\frac{1}{9}$	6

Note. OA, order of Accuracy.

TABLE II

Coefficients for Boundary Formulas at Point 1 (Eq. (14))

Scheme	α_1	a_1	b_1	c_1	d_1	e_1
E4	0	$\frac{-25}{12}$	4	-3	$\frac{4}{3}$	$\frac{-1}{4}$
C4	3	$\frac{-17}{6}$	$\frac{3}{2}$	$\frac{3}{2}$	$\frac{-1}{6}$	0

accuracy of Eq. (13) in the physical plane has been provided previously in Ref. [7] for stretched 1-D meshes.

At boundary points 1, 2, $IL-1$, and IL, higher-order one-sided formulas are utilized which retain the tridiagonal form of the interior scheme. For example, at points 1 and 2 the general formulas are

$$\begin{aligned} \text{Point 1} \quad \phi_1' + \alpha_1\phi_2' &= \frac{1}{\Delta\xi}(a_1\phi_1 + b_1\phi_2 + c_1\phi_3 + d_1\phi_4 + e_1\phi_5) \\ \text{Point 2} \quad \alpha_2\phi_1' + \phi_2' + \alpha_2\phi_3' &= \frac{1}{\Delta\xi}(a_2\phi_1 + b_2\phi_2 + c_2\phi_3 + d_2\phi_4 + e_2\phi_5). \end{aligned} \tag{14}$$

The coefficients for varying orders of accuracy can be obtained through the Taylor series term-matching procedure. Coefficients of schemes employed in this paper are presented in Tables II and III, respectively, and a complete listing is provided in Ref. [14].

The derivatives of the inviscid fluxes are obtained by first forming the fluxes at the nodes and subsequently differentiating each component with the above formulas. For the computation of the viscous terms, the primitive variables, u, v, w, T, are first differentiated to form the components of the stress tensor and the heat flux vector at each node. The viscous flux derivatives are then computed by a second application of the same scheme. This approach was previously shown [6] to provide sufficient accuracy and stability when the scheme is augmented with the filtering procedure described below. We note that more compact high-order midpoint formulas presented in Ref. [14] provide an alternative technique. However, it is more expensive to implement due to the additional high-order interpolation step required.

3.2. Filtering Scheme

Compact-difference discretizations, like other centered schemes, are nondissipative and are therefore susceptible to numerical instabilities due to the growth of high-frequency modes. These difficulties originate mainly from mesh nonuniformity, boundary conditions (see e.g., [15]) and nonlinear flow features. In order to extend the present solver to practical

TABLE III

Coefficients for Boundary Formulas at Point 2 (Eq. (14))

Scheme	α_2	a_2	b_2	c_2	d_2	e_2
E4	0	$\frac{-1}{4}$	$\frac{-5}{6}$	$\frac{3}{2}$	$\frac{-1}{2}$	$\frac{1}{12}$
C4	$\frac{1}{4}$	$\frac{-3}{4}$	0	$\frac{3}{4}$	0	0
C5	$\frac{3}{14}$	$\frac{-19}{28}$	$\frac{-5}{42}$	$\frac{6}{7}$	$\frac{-1}{14}$	$\frac{1}{84}$

TABLE IV
Coefficients for Filter Formula (Eq. (15)) at Interior Points [7]

Scheme	a_0	a_1	a_2	a_3	a_4	a_5	OA
F2	$\frac{1}{2}+\alpha_f$	$\frac{1}{2}+\alpha_f$	0	0	0	0	2
F4	$\frac{5}{8}+\frac{3\alpha_f}{4}$	$\frac{1}{2}+\alpha_f$	$\frac{-1}{8}+\frac{\alpha_f}{4}$	0	0	0	4
F6	$\frac{11}{16}+\frac{5\alpha_f}{8}$	$\frac{15}{32}+\frac{17\alpha_f}{16}$	$\frac{-3}{16}+\frac{3\alpha_f}{8}$	$\frac{1}{32}-\frac{\alpha_f}{16}$	0	0	6
F8	$\frac{93+70\alpha_f}{128}$	$\frac{7+18\alpha_f}{16}$	$\frac{-7+14\alpha_f}{32}$	$\frac{1}{16}-\frac{\alpha_f}{8}$	$\frac{-1}{128}+\frac{\alpha_f}{64}$	0	8
F10	$\frac{193+126\alpha_f}{256}$	$\frac{105+302\alpha_f}{256}$	$\frac{15(-1+2\alpha_f)}{64}$	$\frac{45(1-2\alpha_f)}{512}$	$\frac{5(-1+2\alpha_f)}{256}$	$\frac{1-2\alpha_f}{512}$	10

Note. α_f is a free parameter in the range $0 < |\alpha_f| \leq 0.5$.

simulations, at least those not involving strong stationary shocks, while retaining the improved accuracy of the spatial compact discretization, a high-order implicit filtering technique [6, 7] is incorporated.

If a component of the solution vector is denoted by ϕ, filtered values $\hat{\phi}$ are obtained by solving the tridiagonal system

$$\alpha_f \hat{\phi}_{i-1} + \hat{\phi}_i + \alpha_f \hat{\phi}_{i+1} = \sum_{n=0}^{N} \frac{a_n}{2}(\phi_{i+n} + \phi_{i-n}). \tag{15}$$

Equation (15) is based on templates proposed in Refs. [2, 16] and with proper choice of coefficients, provides a $2N$th-order formula on a $2N+1$ point stencil. The $N+1$ coefficients, $a_0, a_1, \ldots a_N$, are derived in terms of α_f with Taylor- and Fourier-series analyses and for completeness are presented in Table IV. References [6, 7, 17] contain spectral responses of these filters. The adjustable parameter α_f satisfies the inequality $-0.5 < \alpha_f \leq 0.5$, with higher values of α_f corresponding to a less dissipative filter. Extensive numerical experience suggests that regardless of time-integration scheme, values of α_f between 0.3 and 0.5 are appropriate. However, in extremely poor quality meshes, a lower value, $\alpha_f \sim 0.1$ may be required. The filter is typically chosen to be at least two orders of accuracy higher than the difference scheme.

Special formulas are required at near boundary points due to the relatively large stencil of the filter. Values at the end points 1 and IL are not filtered while at other near boundary points, where Eq. (15) cannot be applied, two approaches are suitable. In the first method, proposed in Ref. [6], the order of accuracy is reduced upon approaching the boundary to a level for which a centered scheme is available. Absolute accuracy is retained by optimizing the value of α_f. This approach is particularly suited to problems where the mesh is highly refined near the boundary. The second method, introduced in Ref. [17], employs higher-order one-sided formulas, which again retain the tridiagonal form of the scheme. In this effort, the latter approach is followed.

At a near-boundary point, i, a filter formula is given by

$$\alpha_f \hat{\phi}_{i-1} + \hat{\phi}_i + \alpha_f \hat{\phi}_{i+1} = \sum_{n=1}^{11} a_{n,i} \phi_n \quad i \in \{2, \ldots, 5\}$$

$$\alpha_f \hat{\phi}_{i-1} + \hat{\phi}_i + \alpha_f \hat{\phi}_{i+1} = \sum_{n=0}^{10} a_{IL-n,i} \phi_{IL-n}, \quad i \in \{IL-4, \ldots, IL-1\}. \tag{16}$$

TABLE V

Coefficients for Sixth-Order Boundary Filter Formula at Point 3 (Eq. (16))

OA	$a_{1,3}$	$a_{2,3}$	$a_{3,3}$	$a_{4,3}$	$a_{5,3}$	$a_{6,3}$	$a_{7,3}$
6	$-\frac{1}{64}+\frac{\alpha_f}{32}$	$\frac{3}{32}+\frac{13\alpha_f}{16}$	$\frac{49}{64}+\frac{15\alpha_f}{32}$	$\frac{5}{16}+\frac{3\alpha_f}{8}$	$-\frac{15}{64}+\frac{15\alpha_f}{32}$	$\frac{3}{32}-\frac{3\alpha_f}{16}$	$-\frac{1}{64}+\frac{\alpha_f}{32}$

This choice retains the tridiagonal form of the filter, and α_f remains as the only free parameter. Tables V and VI list coefficients for the higher-order one-sided left-boundary filter formulas employed in the present computations at points 2 and 3. The right-boundary formulas are obtained by noting $a_{IL-n,i} = a_{n+1,IL-i+1}$ for $i \in \{IL-4, \ldots, IL-1\}$. An extensive listing of boundary filter coefficients is provided in [14, 17].

The filter is applied to the conserved variable and sequentially in each coordinate direction. Although the frequency of application can be varied, for the results below, the solution is filtered once after the final stage of the explicit Runge–Kutta method or after each sub-iteration of the implicit algorithm. Where pertinent, the interior filter formula utilized is denoted by appending its designation to that of the scheme. For example, *C6F10*$^{0.4}$ denotes the sixth-order compact method combined with a tenth-order filter ($\alpha_f = 0.4$).

3.3. Time Integration

Two different time-integration approaches are examined. For wave propagation applications, the equations are integrated in time with the classical fourth-order four-stage Runge–Kutta method (*RK4*). With R denoting the residual, the governing equation is

$$\frac{\partial \vec{U}}{\partial t} = R = -J\left(\frac{\partial \hat{F}}{\partial \xi} + \frac{\partial \hat{G}}{\partial \eta} + \frac{\partial \hat{H}}{\partial \zeta} - \frac{1}{Re}\left[\frac{\partial \hat{F}_v}{\partial \xi} + \frac{\partial \hat{G}_v}{\partial \eta} + \frac{\partial \hat{H}_v}{\partial \zeta}\right] + \vec{U}(1/J)_\tau\right). \quad (17)$$

The classical four-stage method, incorporated in the low storage form of Ref. [18], integrates from time t_0 (step n) to $t_0 + \Delta t$ (step $n+1$) through the operations

$$\begin{aligned} k_0 &= \Delta t R(\vec{U}_0) \quad k_1 = \Delta t R(\vec{U}_1) \\ k_2 &= \Delta t R(\vec{U}_2) \quad k_3 = \Delta t R(\vec{U}_3) \\ \vec{U}^{n+1} &= \vec{U} + \frac{1}{6}(k_0 + 2k_1 + 2k_2 + k_3), \end{aligned} \quad (18)$$

TABLE VI

Coefficients for Boundary Filter Formulas at Point 2 (Eq. (16))

OA	$a_{1,2}$	$a_{2,2}$	$a_{3,2}$	$a_{4,2}$	$a_{5,2}$	$a_{6,2}$	$a_{7,2}$
4	$\frac{1}{16}+\frac{7\alpha_f}{8}$	$\frac{3}{4}+\frac{\alpha_f}{2}$	$\frac{3}{8}+\frac{\alpha_f}{4}$	$-\frac{1}{4}+\frac{\alpha_f}{2}$	$\frac{1}{16}-\frac{\alpha_f}{8}$	0	0
6	$\frac{1}{64}+\frac{31\alpha_f}{32}$	$\frac{29}{32}+\frac{3\alpha_f}{16}$	$\frac{15}{64}+\frac{17\alpha_f}{32}$	$-\frac{5}{16}+\frac{5\alpha_f}{8}$	$\frac{15}{64}-\frac{15\alpha_f}{32}$	$-\frac{3}{32}+\frac{3\alpha_f}{16}$	$\frac{1}{64}-\frac{\alpha_f}{32}$

where $\vec{U}_0 = \vec{U}(\xi, \eta, \zeta, \tau)$, $\vec{U}_1 = \vec{U}_0 + k_0/2$, $\vec{U}_2 = \vec{U}_1 + k_1/2$, $\vec{U}_3 = \vec{U}_2 + k_2$. The *RK4* method is employed in the present work only for cases in which the grid coordinates are known as a function of time. In this situation, and for simplicity, the spatial metrics and grid speeds are set to their $n+1$ values.

For problems which demand the use of extremely fine resolution for example, in wall-bounded viscous flows, the stability constraint of the explicit time-marching scheme is found to render the approach too restrictive and inefficient. Therefore, the implicit, approximately-factored method of Beam and Warming [19] is also incorporated and augmented through the use of Newton-like subiterations in order to achieve second-order time accuracy. In delta form, the scheme may be written as

$$\begin{aligned}
&\left[J^{-1^{p+1}} + \phi^i \Delta\tau \delta_\xi^{(2)}\left(\frac{\partial \hat{F}^p}{\partial \vec{U}} - \frac{1}{Re}\frac{\partial \hat{F}_v^p}{\partial \vec{U}}\right)\right] J^{p+1}\\
&\quad\times\left[J^{-1^{p+1}} + \phi^i \Delta\tau \delta_\eta^{(2)}\left(\frac{\partial \hat{G}^p}{\partial \vec{U}} - \frac{1}{Re}\frac{\partial \hat{G}_v^p}{\partial \vec{U}}\right)\right] J^{p+1}\\
&\quad\times\left[J^{-1^{p+1}} + \phi^i \Delta\tau \delta_\zeta^{(2)}\left(\frac{\partial \hat{H}^p}{\partial \vec{U}} - \frac{1}{Re}\frac{\partial \hat{H}_v^p}{\partial \vec{U}}\right)\right] \Delta\vec{U}\\
&= -\phi^i \Delta\tau \left[J^{-1^{p+1}} \frac{(1+\phi)\vec{U}^p - (1+2\phi)\vec{U}^n + \phi\vec{U}^{n-1}}{\Delta\tau} + \vec{U}^p (1/J)_\tau^p\right.\\
&\quad\left. + \delta_\xi\left(\hat{F}^p - \frac{1}{Re}\hat{F}_v^p\right) + \delta_\eta\left(\hat{G}^p - \frac{1}{Re}\hat{G}_v^p\right) + \delta_\zeta\left(\hat{H}^p - \frac{1}{Re}\hat{H}_v^p\right)\right], \qquad (19)
\end{aligned}$$

where

$$\phi^i = \frac{1}{1+\phi}, \quad \Delta\vec{U} = \vec{U}^{p+1} - \vec{U}^p. \qquad (20)$$

$\phi = 0$ and $\phi = 1/2$ yield the Euler-implicit and three-point backward schemes, respectively. For the first subiteration, $p = 1$, $\vec{U}^p = \vec{U}^n$, and as $p \to \infty$, $\vec{U}^p \to \vec{U}^{n+1}$. The spatial derivatives in the implicit operators are represented using standard second-order centered approximations whereas high-order discretizations are employed for the residual. Although not shown in Eq. (19), nonlinear artificial dissipation terms are appended to the implicit operator (only) to enhance stability. These terms, taken from [20], include both second- and fourth-order dissipation operators scaled by the spectral radius. In addition, for improved efficiency, the approximately factored scheme is recast in diagonalized form [21]. The fourth-order implicit damping then gives rise to a scalar pentadiagonal system. Errors due to linearization, diagonalization, and explicit boundary condition implementation are eliminated through the use of subiterations. This also eliminates the impact of the implicit damping coefficients on the final solution. Thus, these coefficients can be chosen exclusively from stability considerations. Typically, three subiterations are applied per time step.

4. RESULTS

4.1. Mesh Quality Issues

Mesh nonuniformities are a major source of error in finite-difference formulations. In Ref. [6], the accuracy of compact-difference-based schemes was investigated on 2-D curvilinear discretizations. Although the grids were highly skewed and stretched, they were nevertheless smoothly generated. In some practical situations, for example, where a surface slope exhibits a discontinuity, the mesh spacing can vary in a sudden manner. The effect of such grid distortions on accuracy and stability of compact-difference schemes, complemented with the higher-order low-pass filter, is now investigated with the goal of establishing procedures to retain the superior performance of higher-order discretizations.

4.1.1. *Effect of Localized Mesh-Spacing Discontinuities*

The impact of localized jumps in mesh spacing on the performance of the high-order discretizations is examined first. A problem suitable for examining the issues involved in a controlled setting is that consisting of a vortex convecting in an otherwise uniform inviscid subsonic flow [6, 22].

The initial flow condition is imposed by prescribing a vortex, centered about the location (x_c, y_c), and satisfying the relations [22]

$$\begin{aligned} u &= 1 - \frac{C(y-y_c)}{R^2}\exp(-r^2/2) \\ v &= \frac{C(x-x_c)}{R^2}\exp(-r^2/2) \\ p_\infty - p &= \frac{\rho C^2}{2R^2}\exp(-r^2) \\ r^2 &= \frac{(x-x_c)^2+(y-y_c)^2}{R^2}, \end{aligned}$$

where u, v, p, and R denote the Cartesian velocity components, static pressure, and vortex core radius, respectively. The nondimensional vortex strength parameter $C/(U_\infty R)$ was chosen to be 0.02 and the freestream Mach number M_∞ was set to 0.1. The relation for pressure was obtained by integration of $\partial p/\partial r = \rho u_\theta^2/r$ about the vortex center. The density was assumed constant, which is suitable for the effectively incompressible flow considered.

The computational grid, spanning the domain $-8 \le x \le 8$; $-8 \le y \le 8$, is shown in Fig. 1a. Abrupt changes are imposed in the streamwise spatial distribution at $x = -4$ (S_1) and $x = 4$ (S_2). At location S_1, the mesh spacing is suddenly halved from $\Delta x_2 = 0.4$ to $\Delta x_1 = 0.2$. Conversely, at S_2, the mesh is abruptly coarsened back to Δx_2. Periodic boundary conditions are applied in both coordinate directions. The grid is uniform in y with $\Delta y = \Delta x_1$. It should be noted that no special treatment is invoked at stations S_1, S_2, and that the flow is computed in a single domain using a general coordinate transformation. At $t = 0$, the vortex is centered at $x = 0$ (Fig. 1b). The computation is then carried out until $t = 16$ at which time the vortex has returned to its initial location following the passage

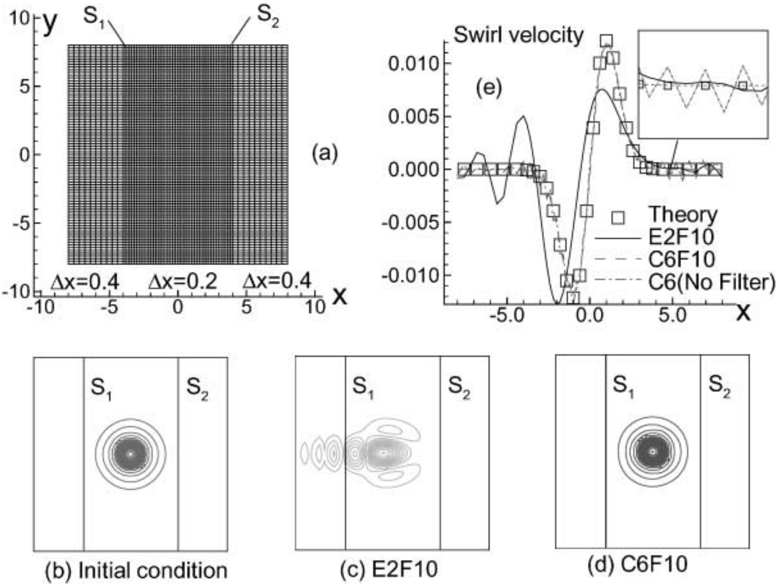

(b) Initial condition (c) E2F10 (d) C6F10

FIG. 1. Performance of compact schemes on a mesh with sudden jumps in grid spacing.

through a sudden mesh coarsening (S_2) and an abrupt grid refinement (S_1). Figures 1c and 1d compare vorticity magnitude contours obtained with *E2* and *C6*, both with filter $F10^{0.49}$, to the exact solution (Fig. 1b). The swirl velocity along the horizontal centerline is plotted in Fig. 1e. It can be seen that the compact scheme combined with the high-order implicit filter retains its superior accuracy despite the localized, high grid stretching. The importance of the filter in suppressing spurious grid-induced oscillations is highlighted by recomputing the same case without the use of a filter. As the last curve in Fig. 1e indicates, the numerical solution develops undesirable high-frequency spatial oscillations which grow unbounded and which are not observed in the filtered results. This behavior is in qualitative agreement with the analysis of Vichnevetsky [5] for the propagation of finite-difference solutions to the one-dimensional advection equation in the presence of localized grid coarsening/refinement. As shown in Ref. [5], passage of a smooth function through sudden mesh coarsening generates spurious high-frequency modes which propagate upstream. If left unfiltered, these spurious oscillations eventually contaminate the entire solution, particularly after interacting with the boundaries of the computational domain.

Calculations were performed with successively refined meshes while retaining the same localized stretch factor of two at the stations S_1, S_2. Figure 2 displays the maximum error (L_∞ norm) in the computed vertical velocity component along the horizontal line passing through the center of the vortex. The superior absolute accuracy of the high-order scheme (*C6*) over the standard second-order method (*E2*) is evident for all values of Δx_1 considered. Although the order of accuracy of the sixth-order scheme is diminished due to the sudden jump in the mesh spacing, extensive calculations presented in Ref. [6], with large but smooth metric variations, have shown that order of accuracy is preserved on curvilinear meshes. In order to explore the issue of stability, calculations with the *C6F8* scheme were extended to $t = 96$. Despite the jumps in grid spacing and the long integration time, no instabilities are observed.

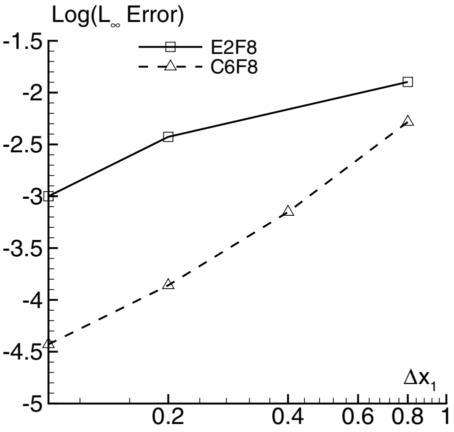

FIG. 2. Effect of grid resolution on maximum error in swirl velocity for mesh with sudden jump in grid spacing.

4.1.2. *Effect of Localized Abrupt Grid Skewing*

The behavior of compact schemes is examined next for the mesh shown in Fig. 3a, which exhibits a localized abrupt change in slope of 25° at $x = 4$. The vortex is convected from its initial location centered at $x = 0$, past the slope discontinuity to its final position $x = 8$ at $t = 8$. Results on a relatively coarse mesh ($\Delta x_o = \Delta y_o = 0.4$), obtained with schemes *E2F8* and *C6F8* using *RK4* and $\Delta t = 0.002$, are displayed in Figs. 3c through 3e. It should be noted that calculations without the inclusion of a filter (not shown) again result in the generation of spurious spatial oscillations which appear as the vortex core reaches the location of sudden mesh skewing and which subsequently contaminate the flow field. Vorticity magnitude contours show that the compact discretization (in conjunction with the high-order filter), Fig. 3d, is once again superior to the standard second-order scheme, Fig. 3c, when compared to the exact solution, Fig. 3b. A more quantitative comparison of

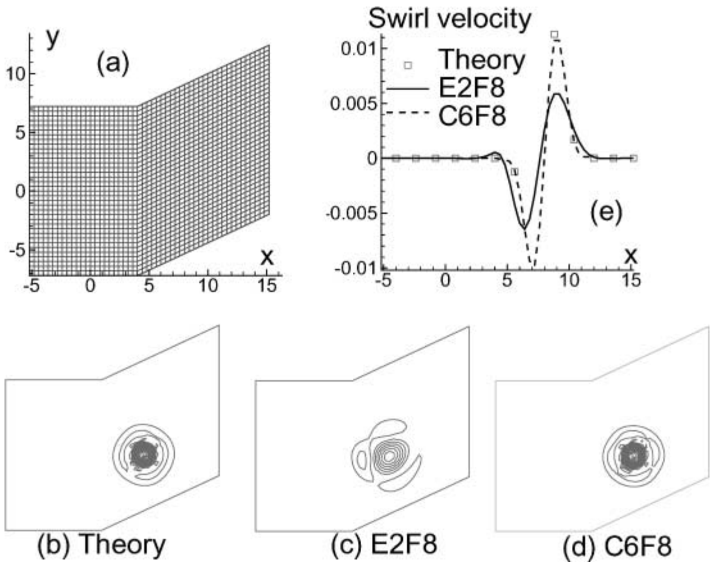

(b) Theory (c) E2F8 (d) C6F8

FIG. 3. Performance of compact schemes on mesh with abrupt grid skewing.

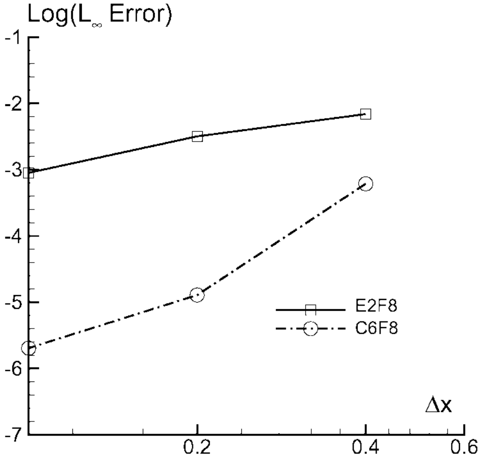

FIG. 4. Effect of grid resolution on maximum error in swirl velocity for mesh with abrupt grid skewing.

the swirl-velocity component along an η-constant coordinate line passing approximately through the vortex center is presented in Fig. 3e and displays excellent agreement between the results computed with *C6F8* and the theoretical distribution. The behavior of both schemes for various levels of spatial resolution is given in Fig. 4 in terms of the maximum error of the computed v-velocity component. Results with *C6* on the coarsest mesh are observed to be more accurate than those obtained with *E2* on the finest mesh, which contains 16 times more points.

4.1.3. *Sensitivity to Mesh Distortion*

As an extreme example of a nonuniform grid, consider the "randomized" mesh of Fig. 5a. A nominal 50×50 uniform mesh is generated in the domain $-6 \leq x \leq 6$, $-6 \leq y \leq 6$.

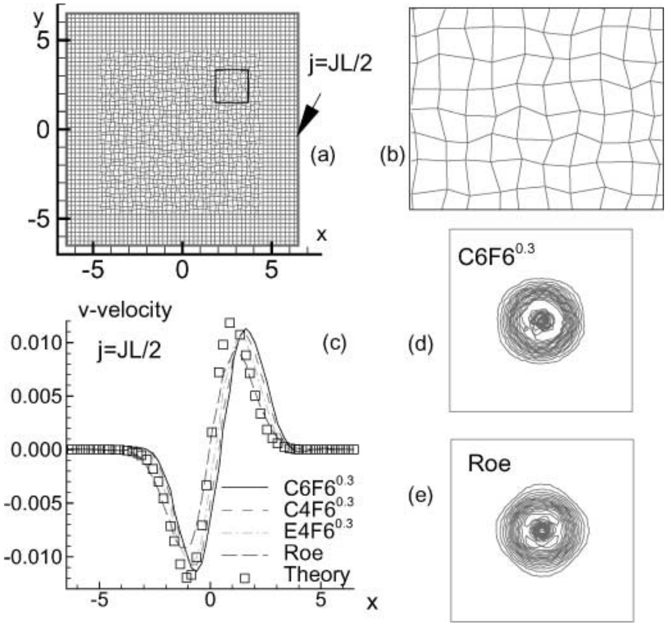

FIG. 5. Performance of compact schemes on randomized mesh.

Interior points are then perturbed by 20% of the nominal spacing in a randomly chosen direction. Note that several points near the boundaries are left unperturbed to provide a high degree of metric continuity at the edges of the domain thereby facilitating implementation of periodic boundary conditions. The resultant mesh, shown in the detail of Fig. 5b, exhibits rapid and persistent nonsmooth metric variations and may be considered a challenging problem for spatially implicit schemes. Computations with both the compact *C4* and the explicit *E4* scheme were found to be unstable without filtering even at extremely small time steps. The most likely cause of this instability is the rapid mesh distortion which can destabilize the computation even in the absence of boundary approximations. Stronger filters than those employed for the above cases are essential to enforce stability; in this case, the sixth-order filter $F6^{0.3}$ was employed. In this event, Fig. 5c indicates that the filter becomes the most dominant aspect of the scheme and the advantage of compact schemes over equal-order explicit schemes is lost for such randomized distorted meshes. However, even with this robust filter, the centered schemes are superior to the Roe flux-difference split nominally third-order upwind-biased scheme. The perturbation velocity contours (Figs. 5d and 5e) also demonstrate less distortion with the compact scheme. Interestingly, the centered scheme exhibits a lead error rather than the usually observed lag error. This is likely attributable to the filter whose symmetry properties are not preserved on nonuniform meshes.

It is important to reiterate that the hierarchy of schemes arranged in terms of formal accuracy remains unaltered on curvilinear meshes if these are generated in a smoother fashion than in the previous example. Thus, higher-order compact-difference schemes, coupled with appropriate high-order low-pass filters, are superior to same-order explicit and lower-order alternatives, even on meshes where stretching and skewing are significant. This can be illustrated by considering a mesh generated with the formula

$$\begin{aligned}
x_{i,j}(\tau) &= x_{\min} + \Delta x_o\left[(i-1) + A_x \sin(2\pi\omega\tau)\sin\left(\frac{n_x\pi(j-1)\Delta y_o}{L_y} + \frac{i\phi_x}{IL-1}\right)\right] \\
y_{i,j}(\tau) &= y_{\min} + \Delta y_o\left[(j-1) + A_y \sin(2\pi\omega\tau)\sin\left(\frac{n_y\pi(i-1)\Delta x_o}{L_x} + \frac{j\phi_y}{JL-1}\right)\right]
\end{aligned} \tag{21}$$

$$\Delta x_o = \frac{L_x}{IL-1}, \quad \Delta y_o = \frac{L_y}{JL-1}$$
$$1 \le i \le IL, \quad 1 \le j \le JL,$$

where IL, JL denote the number of points in the ξ and η directions, $L_x = x_{\max} - x_{\min}$ and $L_y = y_{\max} - y_{\min}$. For the present case, $IL = JL = 30$, $x_{\min} = y_{\min} = -6$, $x_{\max} = y_{\max} = 6$, $A_x = 1$, $A_y = 2$, $n_x = 6 = n_y = 6$, $\phi_x = \phi_y = 0$ and, to obtain a stationary grid at maximum distortion, $\omega\tau = 1/4$. The mesh, displayed in Figs. 6a and 6b, is of relatively poor quality since the maximum deviation from orthogonality is 81.6 degrees, the ratio of maximum to minimum Jacobians is 6.5 and the maximum stretch factor (measured as the ratio of neighboring Jacobians), is 2.3. Starting at $t = 0$ with initial position $x = 0$, $y = 0$, the vortex is convected through regions of fine but skewed spacing alternating with coarse but nearly orthogonal local distribution. To highlight the properties of the scheme, a mild filter, $F10^{0.49}$, is applied to annihilate the odd–even modes observed in the unfiltered calculation. Figure 6c exhibits the v component of velocity at $t = 12$ along the line $j = JL/2$. It is apparent that the compact-difference based schemes are far more accurate than equal-order-explicit or lower-order schemes. Figures 6d and 6e also show contour plots of perturbation

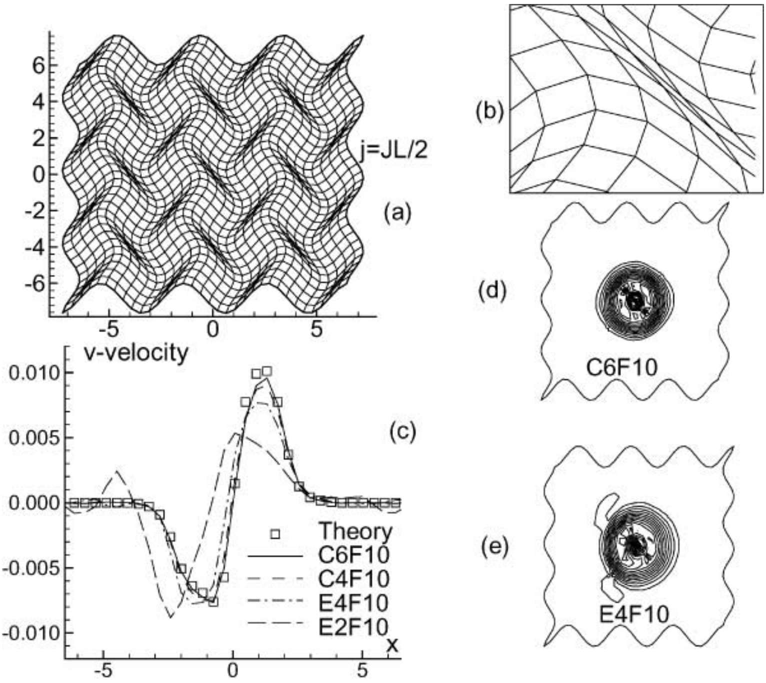

FIG. 6. Performance of compact-difference schemes on a highly distorted mesh.

velocity at $t = 12$ obtained with the *C6* and *E4* schemes and confirm that the former preserves the integrity of the vortex to a much greater degree.

4.2. Freestream Preservation and Metric Cancellation on Stationary 3-D Curvilinear Meshes

The extension of compact schemes to nontrivial 3-D geometries demands that issues of freestream preservation and metric cancellation be addressed. These errors, which arise in finite-difference discretizations of governing equations written in strong-conservation form, can catastrophically destroy the fidelity of both standard and higher-order approaches. In [6], it was shown that on highly distorted curvilinear 2-D meshes, the compact scheme exhibited very small metric cancellation errors when the metrics were evaluated with the same finite-difference expressions as those employed for the fluxes. In 2-D curvilinear grids, the freestream preservation characteristics of the compact scheme are then found to be similar to that of the standard second-order central difference method [12]. Reference [6] also clearly showed that the practice of prescribing *analytic* metrics (when available) on curvilinear meshes can lead to unacceptable errors and therefore should in general be avoided.

As discussed in Refs. [8–10] for the *E2* scheme, the previous straightforward approach of calculating the metrics, although effective in 2-D, fails to provide metric cancellation for general 3-D curvilinear meshes. More specifically, consider the metric relations

$$\begin{aligned} \hat{\xi}_x &= y_\eta z_\zeta - y_\zeta z_\eta \\ \hat{\eta}_x &= y_\zeta z_\xi - y_\xi z_\zeta \\ \hat{\zeta}_x &= y_\xi z_\eta - y_\eta z_\xi . \end{aligned} \tag{22}$$

These may be associated with the x-components of surface area vectors. Corresponding to these is the metric identity I_1 (Eq. (9)), which must be satisfied numerically to ensure freestream preservation. Similar relations exist for the other two components of the surface area vectors. Evaluation of the y and z derivatives in Eq. (22) using explicit or compact centered schemes does not satisfy the identity I_1 and therefore grid-induced errors appear in regions of large grid variation or near singularities. To address this problem for low-order schemes, Pulliam and Steger [8] introduced a simple averaging procedure while Vinokur [9] also proposed the use of finite-volume concepts. These approaches, which work very well for the second-order scheme, are not readily extendable to compact schemes, and in their present form are not suitable even for explicit higher-order formulations.

An alternate and less known method for enforcing the metric identities was given by Thomas and Lombard [10]. Instead of introducing weighted averaging or invoking geometrical concepts, they rewrite the metric expressions in Eq. (22), prior to discretization in the equivalent "conservative" form

$$\begin{aligned}\hat{\xi}_x &= (y_\eta z)_\zeta - (y_\zeta z)_\eta \\ \hat{\eta}_x &= (y_\zeta z)_\xi - (y_\xi z)_\zeta \\ \hat{\zeta}_x &= (y_\xi z)_\eta - (y_\eta z)_\xi,\end{aligned} \tag{23}$$

with similar relations for the remaining metric terms. This approach was proposed in the context of lower-order methods, but did not become popular because of the relatively simpler averaging procedure of Pulliam and Steger. Although Eq. (23) was not envisaged for use with higher-order or compact-difference-based methods, its "conservative" differential form suggests its viability for the present purpose and is therefore selected for evaluation with the present schemes.

In order to examine metric cancellation errors with this new approach, the three-dimensional curvilinear grid shown in Fig. 7 was generated using the equations

$$\begin{aligned}x_{i,j,k}(\tau) &= x_{\min} + \Delta x_o\left[(i-1) + A_x \sin(2\pi\omega\tau) \right.\\ &\qquad \left. \times \sin\frac{n_{xy}\pi(j-1)\Delta y_o}{L_y} \sin\frac{n_{xz}\pi(k-1)\Delta z_o}{L_z}\right] \\ y_{i,j,k}(\tau) &= y_{\min} + \Delta y_o\left[(j-1) + A_y \sin(2\pi\omega\tau) \right.\\ &\qquad \left. \times \sin\frac{n_{yx}\pi(i-1)\Delta x_o}{L_x} \sin\frac{n_{yz}\pi(k-1)\Delta z_o}{L_z}\right] \\ z_{i,j,k}(\tau) &= z_{\min} + \Delta z_o\left[(k-1) + A_z \sin(2\pi\omega\tau) \right.\\ &\qquad \left. \times \sin\frac{n_{zx}\pi(i-1)\Delta x_o}{L_x} \sin\frac{n_{zy}\pi(j-1)\Delta y_o}{L_y}\right] \\ &i = 1 \ldots IL; \quad j = 1 \ldots JL; \quad k = 1 \ldots KL \\ \Delta x_o &= \frac{L_x}{IL-1}; \quad \Delta y_o = \frac{L_y}{JL-1}; \quad \Delta z_o = \frac{L_z}{KL-1},\end{aligned} \tag{24}$$

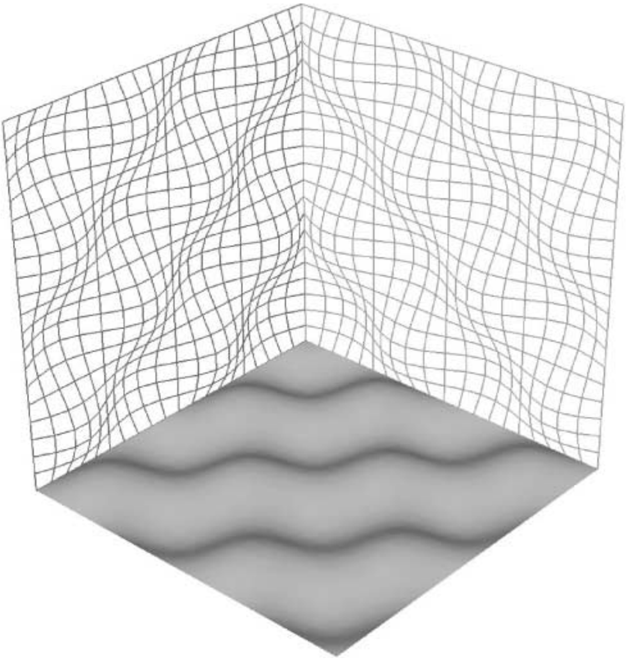

FIG. 7. Three-dimensional wavy mesh.

with the specified parameters $IL = JL = KL = 21$, $A_x = A_y = A_z = 1$, $L_x = L_y = L_z = 4$, and $n_{xy} = n_{yz} = \cdots = 4$ and for this nonmoving mesh case, again $\omega\tau = 1/4$.

Inviscid uniform flow ($u = u_\infty$, $v = w = 0$) was computed on this wavy grid and marched in time for 50 steps ($\Delta t = 0.05$) with a mild $F10^{0.4}$ filter. The maximum departure of v, w from their initial zero values is given in Table VII for various schemes and for two different metric evaluation procedures. When the metrics are computed in the standard manner (i.e., Eq. (22)), significant errors arise for all spatial discretizations in preserving the free stream. It should be noted that the error diminishes when a more accurate scheme is applied. However, the magnitude continues to be unacceptable even for *C6*. In contrast, evaluation of the metric relations using Eq. (23) results in a dramatic reduction of metric cancellation errors for all schemes and guarantees freestream preservation to a suitable degree.

TABLE VII
Freestream Preservation Errors for 3-D Wavy Mesh

	Error (max(v, w))	
Scheme	Standard metrics Eq. (22)	New metrics Eq. (23)
E2	7.3×10^{-1}	2.4×10^{-12}
E4	2.8×10^{-1}	2.3×10^{-12}
C4	6.6×10^{-2}	2.3×10^{-12}
C6	1.1×10^{-2}	2.4×10^{-12}

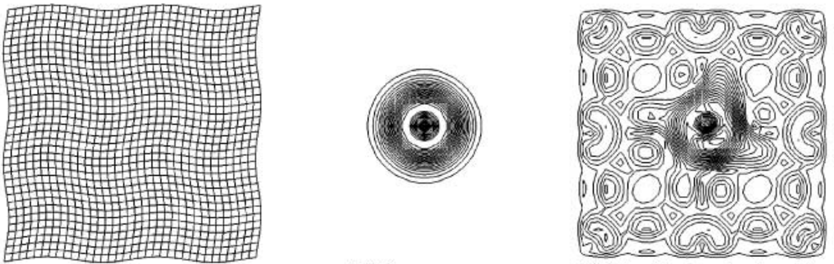

(a) Grid plane (b) Theory (c) E4 with standard metrics

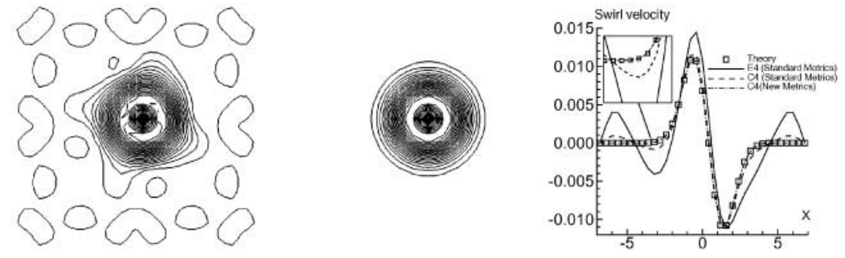

(d) C4 with standard metrics (e) C4 with new metrics (f) Swirl velocity

FIG. 8. Effect of metric evaluation formulas on vortex preservation in a 3-D wavy mesh.

In order to examine the effects of metric cancellation errors on a nontrivial flow, the case of a stationary vortex was computed on another 3-D wavy grid. A less distorted mesh, of which a constant ζ-plane is shown in Fig. 8a, was constructed using Eq. (24) with the following parameters: $IL = JL = 31$, $KL = 21$, $L_x = L_y = 12$, $L_z = 4$, $A_x = A_y = A_z = 0.4$, $n_{xy} = n_{xz} = \cdots = 4$ and $\omega\tau = 1/4$. The initial condition is shown in Figs. 8b and 8f in terms of contours of velocity magnitude and the velocity profile along a j-constant line. When standard metrics are employed, spurious grid-induced structures appear (Figs. 8c and 8d) throughout the domain resulting in distortion of the original vortex. The degradation is more severe for the explicit *E4* scheme and again is observed to diminish with *C4*. When Eq. (23) is used for the metrics, the initial vortex is preserved by both *E4* and *C4*, as shown in Figs. 8e and 8f for the latter scheme. A summary of the maximum error in swirl velocity corresponding to Fig. 8f is shown in Table VIII for the different spatial discretizations and metric evaluation methods. For the fourth-order schemes, an order of magnitude improvement is observed and even for the highly accurate sixth-order scheme, the error is reduced by a factor of 4 when the new metric evaluation procedure is employed.

TABLE VIII
Maximum Error in Swirl Velocity with Different Schemes and Metric Evaluation Procedures for Vortex on 3-D Wavy Mesh

Scheme	Standard metrics	New metrics
E2	2.96×10^{-03}	2.45×10^{-05}
C4	6.72×10^{-04}	2.38×10^{-05}
C6	8.21×10^{-05}	2.36×10^{-05}

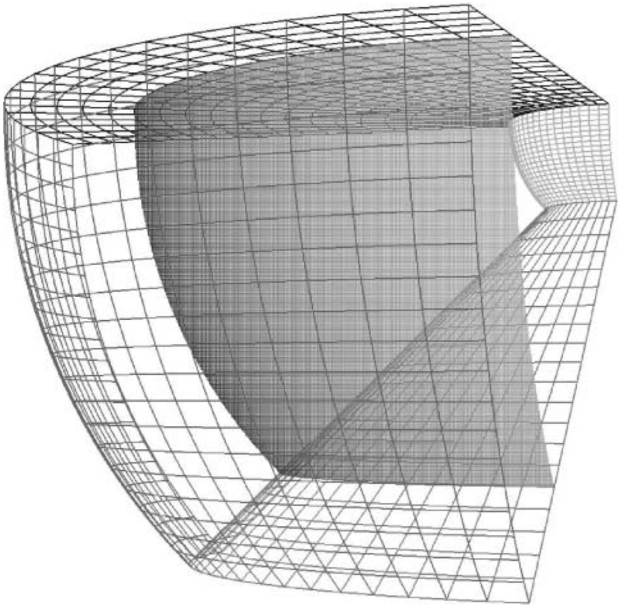

FIG. 9. Grid for spherical sector.

The previous cases clearly demonstrate the importance of proper metric evaluation in higher-order finite-difference approaches for equations written in strong conservation form. The meshes were deliberately selected to highlight these issues but are arguably unrealistically distorted. However, even more commonly encountered meshes exhibit similarly gross error if not treated carefully. As an illustration, consider freestream preservation on the spherical grid shown in Fig. 9. The mesh is generated with uniform Δr, $\Delta\theta$, and $\Delta\phi$ distributions in all directions. Table IX lists metric cancellation errors with several schemes on this relatively benign mesh. Although errors with the standard metrics diminish with increasing order of accuracy, they are still unacceptable for many computations of interest, such as in aeroacoustic, receptivity, and transition simulations. Note also that the use of *analytic* metrics, employed with *C4* for illustration purposes, does not remedy the situation. The new metrics on the other hand preserve the freestream for all practical purposes. The simple and inexpensive modification of Eq. (23) is thus an important step in the extension of higher-order methods to generalized coordinates.

TABLE IX

Freestream Preservation Errors for Spherical Sector

	Error ($\max(v, w)$)		
Scheme	Standard metric Eq. (22)	New metrics Eq. (23)	Analytic metrics
E2	6.0×10^{-2}	9.0×10^{-13}	
E4	1.0×10^{-3}	7.0×10^{-13}	
C4	5.0×10^{-4}	1.4×10^{-12}	3.56×10^{-4}
C6	2.0×10^{-5}	3.9×10^{-12}	

It should be noted that following the present work [17] on the adaptation of the metric form of Thomas and Lombard [10] for use with high-order centered discretizations, Vinokur and Yee [23] have provided a general analytical proof regarding the freestream preservation properties of Eq. (23). They also proposed a more complex coordinate-invariant form for the metric derivatives which was originally given by Thomas and Neier [24].

4.3. Use of Higher-Order Schemes on Deforming and Moving Meshes

For deforming and moving meshes, the *GCL* identity of Eq. (12) must also be satisfied to eliminate metric cancellation errors and to ensure freestream preservation. For the time-integration methods employed in this work (Section 3.3), the time-derivative term in Eq. (1) is split using chain-rule differentiation as follows:

$$(\vec{U}/J)_\tau = (1/J)\vec{U}_\tau + \vec{U}(1/J)_\tau. \tag{25}$$

It should be noted that the above chain-rule differentiation formula does not strictly satisfy strong conservation in time and might not be suitable for rapidly moving strong shocks, which are not considered in the present paper. The first term in Eq. (25) involves the inverse Jacobian, J^{-1}, which is evaluated using the instantaneous values of the grid coordinates in the standard manner:

$$\frac{1}{J} = \begin{vmatrix} x_\xi & y_\xi & z_\xi \\ x_\eta & y_\eta & z_\eta \\ x_\zeta & y_\zeta & z_\zeta \end{vmatrix}. \tag{26}$$

The second term, which includes the time derivative of the inverse Jacobian, requires special treatment. Rather than computing this term directly from the grid coordinates at various time levels (either analytically or numerically), we simply invoke the *GCL* identity (Eq. (12)) to evaluate $(1/J)_\tau$, i.e.,

$$(1/J)_\tau = -[(\hat{\xi}_t)_\xi + (\hat{\eta}_t)_\eta + (\hat{\zeta}_t)_\zeta], \tag{27}$$

where

$$\begin{aligned} \hat{\xi}_t &= -[x_\tau(\hat{\xi}_x) + y_\tau(\hat{\xi}_y) + z_\tau(\hat{\xi}_z)] \\ \hat{\eta}_t &= -[x_\tau(\hat{\eta}_x) + y_\tau(\hat{\eta}_y) + z_\tau(\hat{\eta}_z)] \\ \hat{\zeta}_t &= -[x_\tau(\hat{\zeta}_x) + y_\tau(\hat{\zeta}_y) + z_\tau(\hat{\zeta}_z)]. \end{aligned} \tag{28}$$

For the case of an analytically prescribed dynamic mesh transformation, the grid speeds (x_τ, y_τ, z_τ) appearing in Eq. (28) are obtained from the corresponding analytic expressions. An example in which the grid speeds are known analytically corresponds to the case of a pitching wing when the entire numerical mesh is rotated in a rigid fashion. As the results in Section 4.3.1 will demonstrate, the use of analytic grid speeds (x_τ, y_τ, z_τ) in Eq. (28) effectively provides metric cancellation and freestream preservation. Indeed, the use of I_4 to evaluate the time derivative of the inverse Jacobian compensates for errors introduced in evaluating the other time metrics. To illustrate this, consider the freestream evaluation of the row, R_2, in the residual, Eq. (17), corresponding to the inviscid x-momentum equation:

$$\begin{aligned} R_2 = -J\Big\{&(\rho_\infty u_\infty)\big[\hat{\xi}_{t_\xi} + u_\infty\hat{\xi}_{x_\xi} + v_\infty\hat{\xi}_{y_\xi} + w_\infty\hat{\xi}_{z_\xi}\big] + p\hat{\xi}_{x_\xi} + (\rho_\infty u_\infty)\big[\hat{\eta}_{t_\eta} \\ &+ u_\infty\hat{\eta}_{x_\eta} + v_\infty\hat{\eta}_{y_\eta} + w_\infty\hat{\eta}_{z_\eta}\big] + p\hat{\eta}_{x_\eta} + (\rho_\infty u_\infty)\big[\hat{\zeta}_{t_\zeta} + u_\infty\hat{\zeta}_{x_\zeta} + v_\infty\hat{\zeta}_{y_\zeta} \\ &+ w_\infty\hat{\zeta}_{z_\zeta}\big] + p\hat{\zeta}_{x_\zeta} + (\rho_\infty u_\infty)\left(\frac{1}{J}\right)_\tau\Big\}. \end{aligned} \tag{29}$$

The terms may be regrouped as

$$R_2 = -J\big\{\big(\rho_\infty u_\infty^2 + p\big)I_1 + \rho_\infty u_\infty v_\infty I_2 + \rho_\infty u_\infty w_\infty I_3 + \rho_\infty u_\infty I_4\big\}, \tag{30}$$

where I_1 through I_4 are given in Eqs. (9)–(12), respectively. As noted earlier, if Eq. (23) is employed to evaluate the metrics, identities I_1, I_2, and I_3 are satisfied. Consequently, by utilizing I_4 to explicitly evaluate the time derivative of the transformation Jacobian as in Eq. (27), the last term in Eq. (30) also vanishes, thus extending freestream preservation to deforming meshes. It is important to note that this analysis is independent of the manner in which the grid speeds x_τ, y_τ, and z_τ are obtained (i.e., either analytically or numerically). However, the use of an analytic expression for the *entire* term $(1/J)_\tau$ leads to errors similar to the case of analytic (spatial) metrics as described in Ref. [6]. Since the *GCL* is only employed to compute the time derivative of the inverse Jacobian, this value differs from that which might be obtained directly from the time-varying grid coordinates.

In many practical applications involving deforming meshes (e.g., dynamic aeroelastic simulations), the grid speeds are not known analytically and must therefore be approximated to the desired degree of accuracy with the evolving grid coordinates at several time levels. For this situation, the computed grid speeds are approximated as

$$x_\tau = [(1+\phi)x^{n+1} - (1+2\phi)x^n + \phi x^{n-1}]/\Delta\tau, \tag{31}$$

where $\phi = 0$ or $\phi = \frac{1}{2}$ for first- and second-order temporal accuracy, respectively, with similar approximations for y_τ and z_τ. As demonstrated in the next section, second-order accuracy is found to be suitable, although higher-order approximations are also possible at the expense of more levels of storage for the mesh.

4.3.1. *Dynamically Deforming 2-D Mesh*

In order to test the accuracy of the high-order method for a time-varying curvilinear coordinate transformation, a dynamically deforming "wavy" mesh is first considered. The grid coordinates are specified analytically by Eq. (21) with the parameters $\Delta x_o = \Delta y_o = 0.4$, $A_x = A_y = 3$, $n_x = 8 = n_y = 4$, $\phi_x = \pi$, $\phi_y = \pi/2$. The grid deforms harmonically with a nondimensional frequency $\omega = 1$. At the phase of maximum deformation (Fig. 10a), the mesh has a maximum deviation from orthogonality of approximately 72 degrees and a ratio of maximum to minimum Jacobian of 3.7.

TABLE X
Maximum Freestream Preservation Error $\delta v_{\max} = \max(|\frac{v}{U_\infty}|)$ on Dynamically Deforming 2-D Mesh

Scheme	Time-marching	x_τ, y_τ	$\delta v_{\max}$
E2	*RK4*	Eq. (32)	3.8×10^{-13}
C4F8	*RK4*	Eq. (32)	6.6×10^{-13}
C6F10	*RK4*	Eq. (32)	5.0×10^{-13}
C6F10	*RK4*	Eq. (31), $\phi = 0$	2.7×10^{-13}
C6F10	*RK4*	Eq. (31), $\phi = 1/2$	1.6×10^{-13}
E2	*B-W*	Eq. (32)	2.6×10^{-14}
C6F10	*B-W*	Eq. (32)	2.3×10^{-13}

For this analytically prescribed deforming mesh, the grid speeds can be obtained from Eq. (21) by straightforward differentiation giving

$$\begin{aligned} x_\tau &= 2\pi\omega A_x \Delta x_o \cos(2\pi\omega\tau) \sin\left(\frac{n_x\pi(j-1)\Delta y_o}{L_y} + \frac{i\phi_x}{IL-1}\right) \\ y_\tau &= 2\pi\omega A_y \Delta y_o \cos(2\pi\omega\tau) \sin\left(\frac{n_y\pi(i-1)\Delta x_o}{L_x} + \frac{j\phi_y}{JL-1}\right). \end{aligned} \tag{32}$$

For the parameters specified above, the grid speeds attain a relatively large maximum nondimensional value $(x_\tau)_{\max} = (y_\tau)_{\max} = 3.77$.

To evaluate the freestream preservation properties of the present formulation, inviscid uniform flow ($u = u_\infty$, $v = 0$) was computed on this dynamically deforming wavy mesh. The solution was advanced in time until $\tau = 1.25$ using a time-step size of $\Delta\tau = 0.002$. At this instant, the mesh had undergone 1.25 deformation cycles. Results for the maximum error in v-velocity are summarized in Table X. These results show that the metric cancellation errors on this highly distorted and rapidly moving mesh are very small for both the second- and high-order compact discretizations, as well as for both time-marching schemes. Furthermore, as expected, freestream preservation is practically achieved whether the grid speeds are specified analytically or are calculated using first- or second-order approximations.

In order to examine the accuracy of the high-order method on dynamic meshes, the vortex convection test is computed on the deforming grid given by Eq. (2) (Fig. 10a). Three different levels of resolution are used, corresponding to $\Delta x_o = \Delta y_o = 0.6, 0.4, 0.2$. In all calculations, the vortex is convected from $x = 0$ to $x = 8.25$ using the *RK4* time-integration scheme with $\Delta\tau = 0.002$, which provides 500 steps per grid-oscillation cycle and is sufficiently small to provide essentially time-step-size independent results on the grids considered. During the time of the calculations, the mesh undergoes 8.25 cycles of the prescribed dynamic deformation (Eq. (21), $\omega = 1$). The grid speeds x_τ, y_τ are specified analytically through Eq. (32). Results on the medium mesh using the high-order scheme *C6F10* (Fig. 10b) and the standard second-order method (Fig. 10c) are compared with the exact solution (Fig. 10d) in terms of contours of vorticity magnitude. It is apparent that on this relatively coarse deforming mesh, the high-order approach is capable of convecting the vortex with excellent fidelity. By contrast, the second-order scheme exhibits significant dissipation and distortion of the original vortex. A more quantitative comparison is shown in Fig. 11 using the v velocity component along the $\eta =$ constant line passing

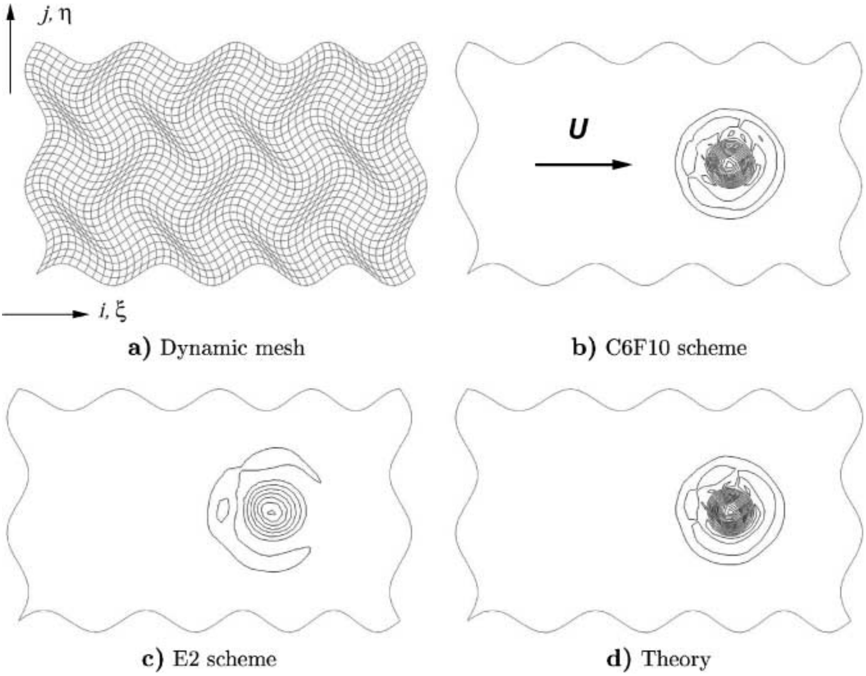

a) Dynamic mesh
b) C6F10 scheme
c) E2 scheme
d) Theory

FIG. 10. Vortex advection on dynamic 2-D mesh.

approximately through the center of the vortex. The superior behavior of the *C6F10* scheme compared to the *E2* approach is clearly retained even under the imposed severe dynamic grid distortion.

The grid-convergence properties of the schemes are shown in Fig. 12, which displays the maximum error (L_∞ norm) in the computed swirl velocity magnitude along the mesh line through the center of the vortex. In terms of absolute error, these results demonstrate that significant improvements can be achieved with the high-order approach in dynamic mesh simulations.

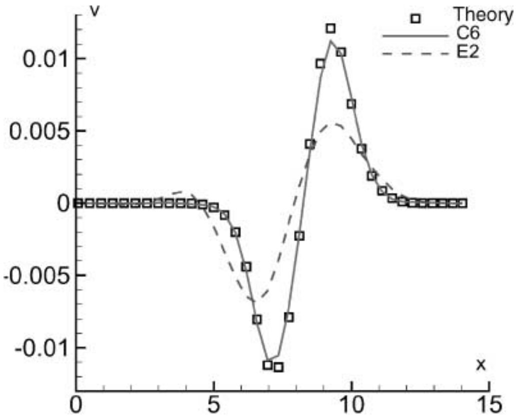

FIG. 11. Effect of spatial discretization for vortex advection on dynamic 2-D mesh.

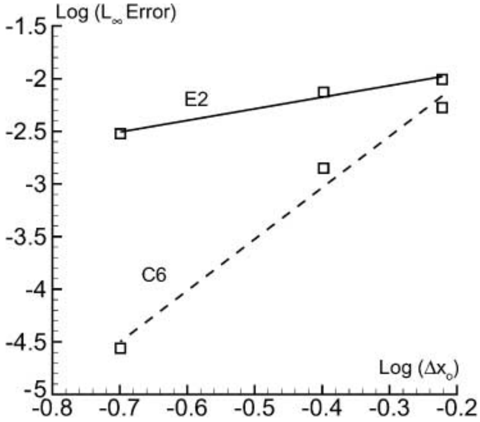

FIG. 12. Effect of grid resolution on maximum error in swirl velocity for dynamic 2-D mesh.

The vortex-advection test case was also employed to assess the impact of grid-speed evaluation method on solution accuracy. For this purpose, the flow was recomputed using numerically determined values for x_τ, y_τ. The error in the computed swirl velocity magnitude within the vortex is shown in Fig. 13 for the *C6F10-RK4* scheme and for different approaches of evaluating the grid speeds, including analytic (Eq. (32)) as well as first- and second-order approximations. When a first-order approximation (Eq. (31), $\phi = 0$) is employed for x_τ, y_τ, minor differences (in terms of the error plot) are observed in comparison with the results obtained with analytic grid speeds. However, these discrepancies are very small and do not yield appreciable differences in swirl velocity. The error curves corresponding to second-order (Eq. (31), $\phi = \frac{1}{2}$) and analytic grid speeds are found to be essentially the same. Therefore, higher-order approximations for computing the grid speeds were not deemed necessary.

Finally, the effect of time-integration scheme was evaluated for the vortex convection simulation on the dynamically deforming mesh. Calculations were performed on the finest level of spatial resolution ($\Delta x_o = \Delta y_o = 0.2$) using the *C6F10* scheme and both the explicit

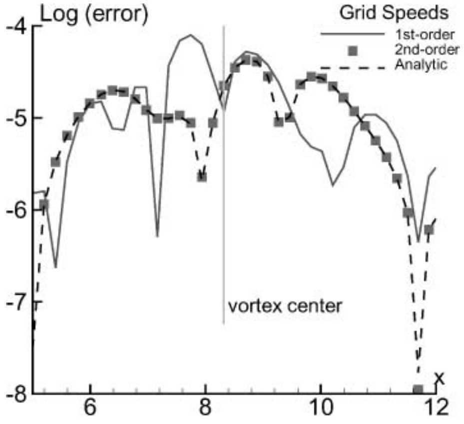

FIG. 13. Effect of grid speed evaluation procedure on swirl velocity error for vortex advection on dynamic 2-D mesh.

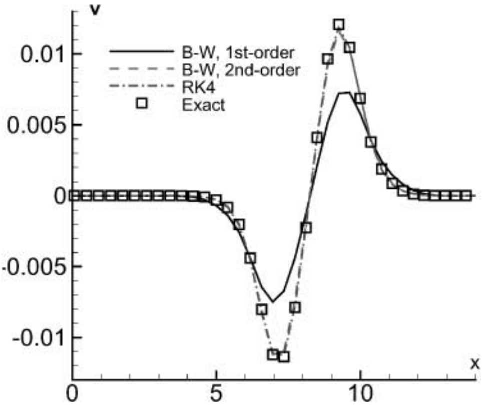

FIG. 14. Effect of time-integration scheme for vortex advection on dynamic 2-D mesh.

and implicit time-marching methods. The time-step size was increased to $\Delta\tau = 0.01$ which corresponds to only 100 steps per cycle of deformation of the mesh. As shown in Fig. 14, results obtained with the first-order Beam–Warming scheme (in conjunction with first-order grid speeds) were found to be in poor agreement with the exact solution. The computed swirl velocity remained essentially unchanged when analytic grid speeds were specified along with the first-order time-marching implicit method (not shown). This indicates that the poor performance of the first-order Beam–Warming method is not attributable to the grid-speed evaluation procedure but rather to the lower order of accuracy of the time-marching scheme. The swirl velocity computed with the second-order Beam–Warming scheme (with second-order numerical grid speeds) is found to be in excellent agreement with the corresponding results for *RK4* (with analytic grid speeds), as well as with the exact solution. Based on the good characteristics of the second-order subiterative Beam–Warming method for this relatively large time-step size, higher-order implicit time-marching approaches were not pursued. It should also be noted that further improvements in time accuracy could be achieved within the context of the present iterative approach by replacing the physical time-derivative, appearing on the right-hand-side of Eq. (19), with a higher-order approximation (at the expense, of course, of additional levels of storage for the deforming grid coordinates and the dependent variables).

4.3.2. *Dynamically Deforming 3-D Mesh*

In order to test the behavior of the high-order scheme for 3-D dynamic curvilinear grids, a deforming wavy mesh (similar to that in Fig. 7) was constructed using Eq. (24) with the specified parameters $IL = JL = KL = 31$, $A_x = A_y = A_z = 1.5$, $L_x = L_y = L_z = 12$, and $n_{xy} = n_{yz} = \cdots = 4$, and frequency of oscillation $\omega = 1.0$. The grid speeds (x_τ, y_τ, z_τ) were obtained analytically by direct differentiation of Eq. (24). For instance,

$$x_\tau = 2\pi\omega A_x \Delta x_o \cos(2\pi\omega\tau) \sin\frac{n_{xy}\pi(j-1)\Delta y_o}{L_y} \sin\frac{n_{xz}\pi(k-1)\Delta z_o}{L_z}. \tag{33}$$

With the parameters prescribed above, the maximum (nondimensional) speed attained by the grid was 3.77.

TABLE XI
Maximum Freestream Preservation Error max($|\frac{v}{U_\infty}|, |\frac{w}{U_\infty}|$) on Dynamically Deforming 3-D Mesh

Scheme	Standard metrics Eq. (22)	New metrics Eq. (23)
C4F8	1.1×10^{-2}	8.2×10^{-14}
C6F10	3.8×10^{-3}	6.7×10^{-14}

In order to test for freestream preservation, uniform flow ($u = u_\infty$, $v = w = 0$) was computed on this dynamic mesh. The solution was integrated in time with the *RK4* method and $\Delta\tau = 0.002$ up to the phase of maximum distortion of the grid ($\tau = 0.25$). The maximum departure of v, w from their initial zero values is given in Table XI for the *C4F8* and *C6F10* schemes. These results indicate that for this severely distorting 3-D mesh, the high-order compact schemes exhibit freestream preservation when the spatial metrics are computed using Eq. (23), and when the time-derivative of the Jacobian is expressed in terms of the *GCL* identity (Eq. (27)). By contrast, if standard metrics are employed (Eq. (22)), significant metric cancellation errors appear that would invalidate an actual flow solution on this deforming grid.

To evaluate the performance of the high-order approach for a nontrivial flow on the 3-D dynamic mesh, the case of a stationary columnar vortex was considered with the axis of the vortex placed along $z = 0$. Inviscid calculations were performed with the *E2* and *C6* schemes using the *RK4* method and a time step $\Delta\tau = 0.002$. A cross section of the vortex on a ζ = constant plane at $\tau = 3.25$ is shown in Fig. 15a. At this instant, the grid has already experienced more than three cycles of the imposed oscillation with frequency $\omega = 1$. As the contours of velocity magnitude indicate, despite the significant unsteady mesh deformations, the high-order method is capable of preserving the axisymmetric character of the vortex even on this relatively coarse discretization (approximately 10 points across the vortex). A comparison of the computed and exact solutions is shown in Fig. 15b in terms of the v component of velocity. The *C6F10* results are observed to be in excellent

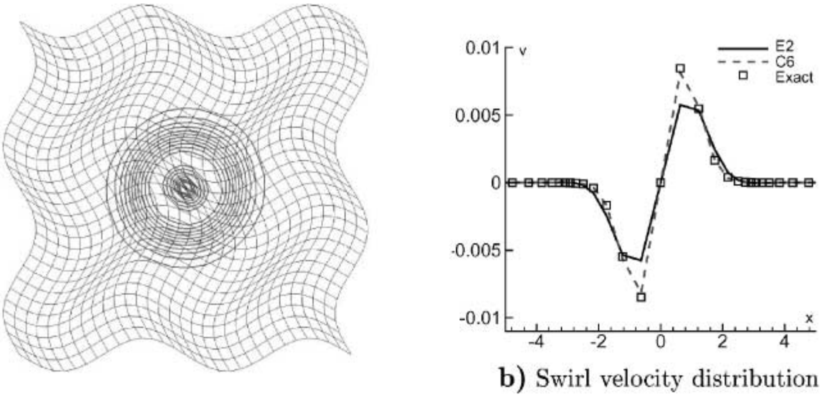

b) Swirl velocity distribution

a) Contours of velocity magnitude on ζ=constant plane

FIG. 15. Stationary vortex preservation on dynamically deforming 3-D mesh.

agreement with the theoretical answer. This case demonstrates the advantage of the high-order methodology over standard low-order approaches even for 3-D applications in which the mesh is subjected to severe dynamic deformation.

4.4. Application to Flow over a Pitching Airfoil

The performance of this newly developed high-order solver for dynamic meshes is demonstrated in this section for the case of viscous laminar flow past a rapidly pitching airfoil. Calculations were performed for a NACA 0012 airfoil pitching at a nominally constant rate from zero incidence to a high angle of attack past the onset of dynamic stall [25]. The pivot axis was located at the airfoil quarter chord. The freestream Mach number and chord Reynolds number were 0.1 and 2.0×10^4, respectively. The airfoil instantaneous pitch rate was given according to the expression [25]

$$\Omega(\tau) = \Omega_o\left(1 - e^{-4.6\tau/\tau_o}\right), \tag{34}$$

where $\Omega_o = 0.2$ denotes the nondimensional pitch rate (based on airfoil chord and u_∞), and $\tau_o = 0.5$ corresponds to the time interval in which the airfoil accelerates to its final angular rate starting from rest.

Computations were performed with the implicit time-marching algorithm since the explicit method became impractical due to the fine mesh spacing employed next to the airfoil surface and around the trailing edge. In all cases, a time step $\Delta\tau = 0.001$ was prescribed along with three subiterations. Results were obtained with the standard second-order and the sixth-order compact formulations. Following Ref. [25], these calculations were first performed employing a rotating rigid grid attached to the airfoil (Fig. 16a). With this approach, the instantaneous grid coordinates (x, y) and grid speeds (x_τ, y_τ) can be computed analytically from the initial mesh at zero angle of attack and the prescribed airfoil motion. Although the analytic value of the time derivative of the Jacobian vanishes for this rigid mesh, Eq. (27) was retained to compute $(1/J)_\tau$ in order to avoid metric cancellation errors. Vorticity contours are displayed in Figs. 16b–16d corresponding to $\tau = 2.25$ and an angle of attack of 24.5 degrees. By this instant, the formation of the leading-edge dynamic stall vortex is apparent. The results obtained with the *C6* scheme on a 203×51 mesh (Fig. 16b) exhibit, in addition to the leading-edge vortex, the formation of several shear-layer vortical structures, as well as induced secondary separation regions underneath. By contrast, on the same mesh, the second-order method fails to properly capture these shear-layer structures (Fig. 16c) even when the spatial resolution above the airfoil upper surface is doubled in both coordinate directions (Fig. 16d).

Pitching airfoil simulations were also performed with the high-order scheme for the more demanding situation in which the computational mesh is deformed in order to accommodate the airfoil pitching motion (Fig. 17a). The mesh was evolved according to the expressions

$$\begin{aligned} x_{i,j}^{n+1} &= x_{i,j}^{n} + \delta x_{i,j} \\ y_{i,j}^{n+1} &= y_{i,j}^{n} + \delta y_{i,j} \\ \delta x_{i,j} &= \delta x_{i,1} G_{i,j}, \quad \delta y_{i,j} = \delta y_{i,1} G_{i,j} \\ G_{i,j} &= 1 - 3g_{i,j}^2 + 2g_{i,j}^3 \\ g_{i,j} &= s_{i,j} \big/ s_{i,j_{\max}}, \quad 1 \le j \le j_{\max}, \end{aligned} \tag{35}$$

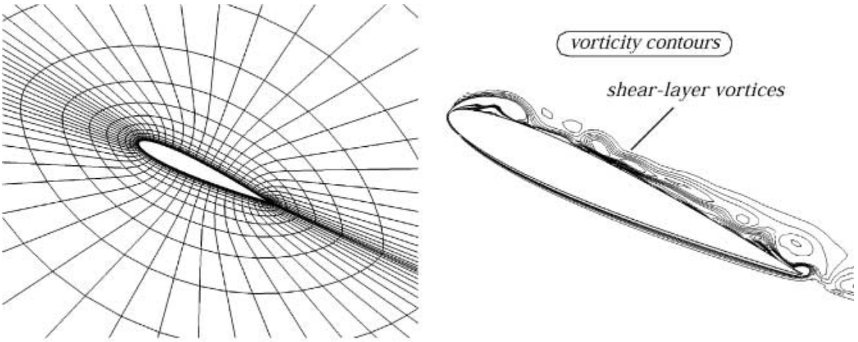

a) rotating rigid grid **b)** C6, 203 × 51 mesh

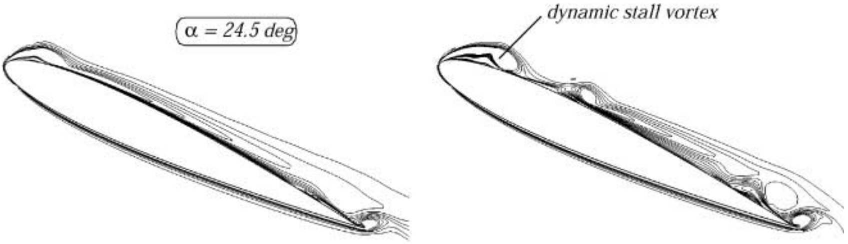

c) E2, 203 × 51 mesh **d)** E2, 260 × 101 mesh

FIG. 16. Computation of flow past a pitching airfoil using a rotating rigid mesh.

where $\delta x_{i,1}, \delta y_{i,1}$ denote the coordinate changes on the airfoil surface, s is the arc-length along the $\xi =$ constant lines, and $j_{\max}$ is the η-location in the farfield beyond which the mesh remains undeformed. The grid speeds were computed numerically with the second-order, three-point backward approximation of Eq. (31). Despite the differences between the grids of Figs. 16a and 17a, as well as the distortions induced near the airfoil surface for

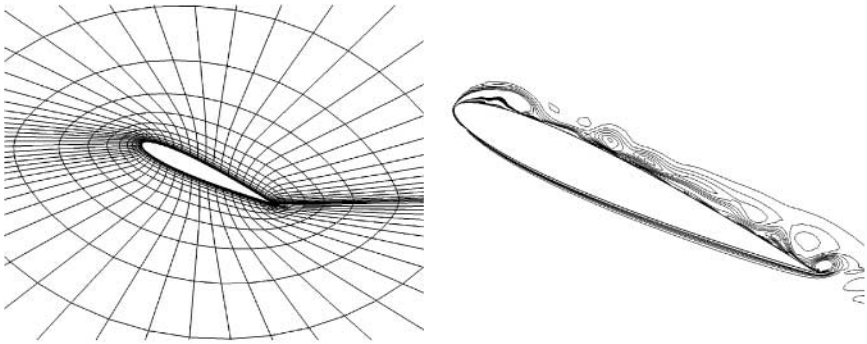

a) Deforming grid **b)** C6 203 × 51

FIG. 17. Computation of flow past a pitching airfoil using a deforming mesh.

the deforming mesh, the vorticity contours obtained with both moving mesh approaches are found to be in good agreement (see Figs. 16b and 17b). This example serves to illustrate the versatility and robustness of the high-order methodology for moving body simulations.

4.5. Application to Boundary-Layer Flow over a Flexible Surface

The last case considered for demonstration of the high-order, dynamic-mesh technique comprises the simulation of the aeroelastic interaction arising from viscous laminar flow over a flexible surface. This problem is closely related to the classic panel flutter phenomenon [26], as well as to boundary-layer flow over compliant surfaces [27]. A schematic of the configuration considered is shown in Fig. 18a. The freestream Mach number and Reynolds number (based on panel length, L) were 0.9 and 1.0×10^5, respectively. The computed boundary-layer thickness at the leading-edge of the flexible panel was approximately $\delta = 0.04L$. The pressure in the cavity underneath the flexible panel was assumed to be fixed at the freestream value p_∞. The flow field was computed using the sixth-order scheme (*C6*) and the second-order, implicit Beam–Warming method (with $\Delta\tau = 0.01$ and four subiterations).

In the present aeroelastic application, the shape of the portion of the lower boundary corresponding to the deforming panel is not known *a priori* as a function of time and must

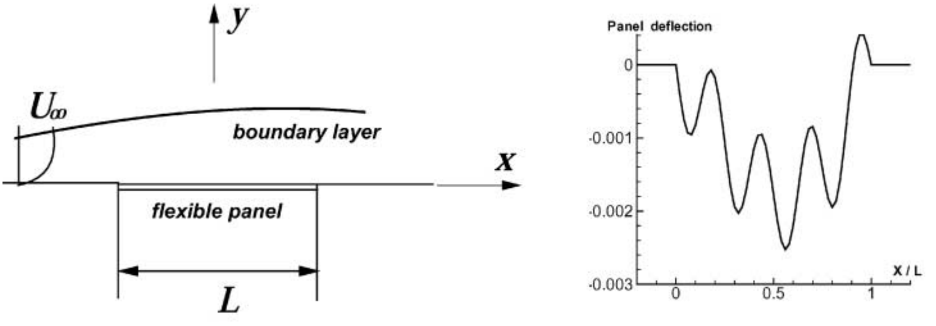

a) Flexible panel configuration **b)** Instantaneous panel deflection

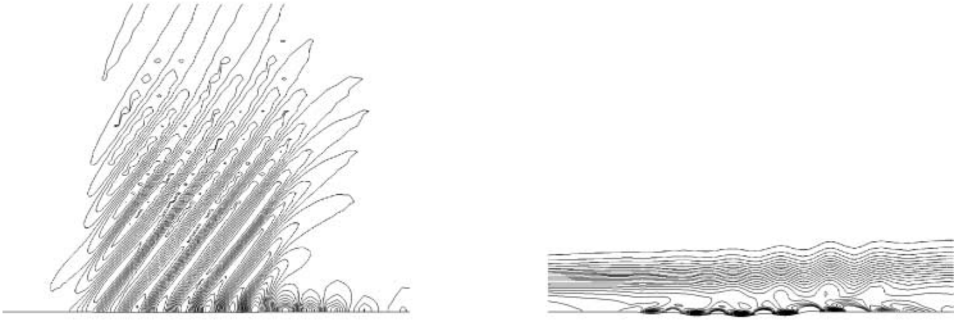

c) Contours of instantaneous pressure above vibrating panel **d)** Instantaneous vorticity contours

FIG. 18. Boundary-layer flow over a flexible panel.

be obtained as part of the solution based on the panel structural response. This response is computed here by solving the (nonlinear) von Karman plate equations, which are required when the magnitudes of the deflections are of the order of the panel thickness. Detailed descriptions of the structural equations, their numerical solution procedure, and the fluid-structural coupling are provided in Ref. [28]. At each subiteration of the implicit time-marching method, the shape of the deforming panel is updated by the structural solver. Based on the new boundary coordinates, the fluid dynamic mesh is evolved by propagating the panel deformations into the entire field using a blending procedure similar to that of Eq. (35). This subiterative approach effectively eliminates lag effects between the fluid and structural modules.

The aeroelastic simulation is started by specifying as the initial condition the computed steady boundary-layer solution over a rigid surface. In order to initiate the fluid/structure interaction, a small vertical velocity in the first-mode is imparted to the panel [28]. Following initial transients, a limit-cycle-oscillation with an approximate nondimensional frequency $St = fL/u_\infty = 1.62$ was achieved by the combined fluid/structural system. A representative plot of the instantaneous panel deflection is shown in Fig. 18b. From this and many other instantaneous realizations of the panel shape (not shown), it became apparent that the panel dynamics comprises a first-mode mean downward deflection upon which a high-mode, high-frequency vertical fluctuation is superimposed. These high-frequency fluctuations result in a significant acoustic radiation pattern above the vibrating panel, shown in Fig. 18c in terms of a snapshot of the instantaneous pressure. Corresponding contours of vorticity are shown in Fig. 18d, with an enlarged scale (by a factor of 8) in the y-direction for the purpose of clarity. Vorticity waves are clearly visible in the boundary layer and appear to roll up and interact with the wall resulting in the formation of secondary incipient separation regions. This aeroelastic computation points out the potential of the present approach for fluid/structure simulations requiring DNS/LES representations of turbulence for which high-order spatial discretizations on moving meshes are necessary.

5. CONCLUSIONS

Several issues have been addressed relating to the use of high-order compact-difference schemes on stretched, curvilinear, and moving/deforming meshes. It has been shown that on stretched and skewed meshes, the discriminating low-pass filtering component is crucial to maintaining the stability and retaining the superior accuracy properties of the higher-order schemes. A "conservative" form of spatial metric evaluation procedure, originally proposed in the context of lower-order methods, has been successfully adopted to ensure that uniform fields are preserved even on highly distorted three-dimensional meshes. This ensures that metric cancellation errors, which have the potential to degrade the accuracy of the solution, are minimized for practical calculations. For moving and dynamically deforming meshes, a procedure has been developed to enforce the geometric conservation law regardless of whether grid speeds are computed analytically or numerically. Based on several test cases performed on highly dynamic meshes, the higher-order approach has been shown to be superior to lower-order methods. These procedures extend the realm of application of the high-order techniques as demonstrated by application to flow over a rapidly pitching airfoil, as well as to limit-cycle-oscillation phenomena arising from viscous flow over a flexible panel. Although these techniques have been developed and demonstrated for compact methods applied to the Navier–Stokes equations, they are equally applicable to other higher-order or optimized finite-difference schemes and to other sets of conservation laws.

ACKNOWLEDGMENTS

The authors are grateful for AFOSR sponsorship under tasks monitored by R. Herklotz, W. Hilbun, and S. Walker. This work was also supported in part by a grant of HPC time from the DoD HPC Shared Resource Centers at CEWES and NAVO.

REFERENCES

1. C. Canuto, M. Y. Hussaini, A. Quarteroni, and T. A. Zang, *Spectral Methods in Fluid Dynamics* (Springer-Verlag, Berlin/New York, 1987).
2. S. K. Lele, Compact finite difference schemes with spectral-like resolution, *J. Comput. Phys.* **103**, 16 (1992).
3. C. K. W. Tam and J. C. Webb, Dispersion-relation-preserving finite difference schemes for computational acoustics, *J. Comput. Phys.* **107**, 262 (1993).
4. C. A. Kennedy and M. H. Carpenter, Several new numerical methods for compressible shear-layer simulations, *Appl. Numer. Math.* **14**(2) (1994).
5. R. Vichnevetsky, Propagation through numerical mesh refinement for hyperbolic equations, *Math. Comp. Simulation* **XXIII**, 344 (1981).
6. M. R. Visbal and D. V. Gaitonde. High-order accurate methods for complex unsteady subsonic flows, *AIAA J.* **37**(10), 1231 (1999).
7. D. V. Gaitonde, J. S. Shang, and J. L. Young, Practical aspects of higher-order numerical schemes for wave propagation phenomena, *Int. J. Numer. Meth. Eng.* **45**, 1849 (1999).
8. T. H. Pulliam and J. L. Steger, Implicit finite-difference simulation of three-dimensional compressible flow, *AIAA J.* **18**(2), 159 (1980).
9. M. Vinokur, An analysis of finite-difference and finite-volume formulations of conservation laws, *J. Comput. Phys.* **81**, 1 (1989).
10. P. D. Thomas and C. K. Lombard, Geometric conservation law and its application to flow computations on moving grids, *AIAA J.* **17**(10), 1030 (1979).
11. M. Vinokur, Conservation equations of gasdynamics in curvilinear coordinate systems, *J. Comput. Phys.* **14**, 105 (1974).
12. J. L. Steger, Implicit finite-difference simulation of flow about arbitrary two-dimensional geometries, *AIAA J.* **16**(7), 679 (1978).
13. D. A. Anderson, J. C. Tannehill, and R. H. Pletcher, *Computational Fluid Mechanics and Heat Transfer* (McGraw–Hill, New York, 1984).
14. D. V. Gaitonde and M. R. Visbal, High-order schemes for Navier–Stokes equations: Algorithm and implementation into FDL3DI. Technical Report AFRL-VA-WP-TR-1998-3060 (Air Force Research Laboratory, Wright-Patterson AFB, 1998).
15. M. H. Carpenter, D. Gottlieb, and S. Abarbanel, The stability of numerical boundary treatments for compact high-order finite-difference schemes, *J. Comput. Phys.* **108**, 272 (1993).
16. P. Alpert, Implicit filtering in conjunction with explicit filtering, *J. Comput. Phys.* **44**, 212 (1981).
17. D. V. Gaitonde and M. R. Visbal, *Further Development of a Navier–Stokes Solution Procedure Based on Higher-Order Formulas*, Technical Paper 99-0557 (AIAA Press, Washington, DC, 1999).
18. D. J. Fyfe, Economical evaluation of Runge–Kutta formulae, *Math. Comput.* **20**, 392 (1966).
19. R. Beam and R. Warming, An implicit factored scheme for the compressible Navier–Stokes equations, *AIAA J.* **16**(4), 393 (1978).
20. T. Pulliam, Artificial dissipation models for the Euler equations, *AIAA J.* **24**(12), 1931 (1986).

21. T. H. Pulliam and D. S. Chaussee, A diagonal form of an implicit approximate-factorization algorithm, *J. Comput. Phys.* **39**(2), 347 (1981).
22. T. J. Poinsot and S. K. Lele, Boundary conditions for direct simulations of compressible viscous flows, *J. Comput. Phys.* **101**, 104 (1992).
23. M. Vinokur and H. C. Yee, Extension of efficient low dissipation high-order schemes for 3-D curvilinear moving grids, Technical Report TM 2000-209598 (NASA, June 2000).
24. P. D. Thomas and K. L. Neier, Navier–Stokes simulation of three-dimensional hypersonic equilibrium flows with ablation, *J. Spacecraft Rockets* **27**(2), 143 (1990).
25. M. R. Visbal and J. S. Shang, Investigation of the flow structure around a rapidly pitching airfoil, *AIAA J.* **27**(8), 1044 (1989).
26. E. H. Dowell, Panel flutter: A review of the aeroelastic stability of plates and shells, *AIAA J.* **8**(3), 385 (1970).
27. M. T. Landahl, On the stability of a laminar incompressible boundary layer over a flexible surface, *JFM* **13**, 609 (1962).
28. R. E. Gordnier and M. R. Visbal, Development of a Three-Dimensional Viscous Aeroelastic Solver for Nonlinear Panel Flutter, Technical Paper 2000-2337 (AIAA Press, Washington, DC, 2000).